Chapter 7

Thin Films and Devices for Perovskite Solar Cells

Publication: ***<u>Manish Kumar</u>,*** *and Prabhakar Singh, Investigation of hole transport/perovskite layer interface for perovskite solar cells (Under Preparation).*

CHAPTER 7: Thin Films and Devices for Perovskite Solar cells

7.1 Introduction

It is already proven in the literature that tin-based perovskite halide is the best alternative to the $CH_3NH_3PbI_3$ [190],[191]. As per the detailed literature survey, there is little experimental and theoretical analysis for tin-based materials. Tin-based materials have shown low V_{oc} and maximum power conversion efficiency is 6.4% [192]. But tin-based Perovskites are unstable in the ambient atmosphere and got easily affected by the oxidation process [193]. Perovskite solar cells are unstable in the ambient atmosphere; those are easily affected by the oxidation process due to the oxidation of Sn^{2+} into Sn^{4+} [194]. The device architecture needs to be optimized for better performance. However, the planar and inverted configurations along with the thickness of the electron transport material, hole transport material, an absorber layer play a crucial layer in the absorbing characteristics [194],[195]. In the present thesis work, the thickness of the three layers (TiO_2, CuO, and $CsPb/SnBr_3$) has been optimized using the Finite Element Modelling technique. Further, a device has been realized using the Pulsed Laser Deposition technique with the optimized thickness from FEM simulations.

7.2 Methodology

COMSOL Multiphysics is being used here to perform the FEM calculations. The morphology being used for the interfacial properties is shown in Fig. 7.1 and the triangular mesh is applied during the measurements (Fig. 7.2).

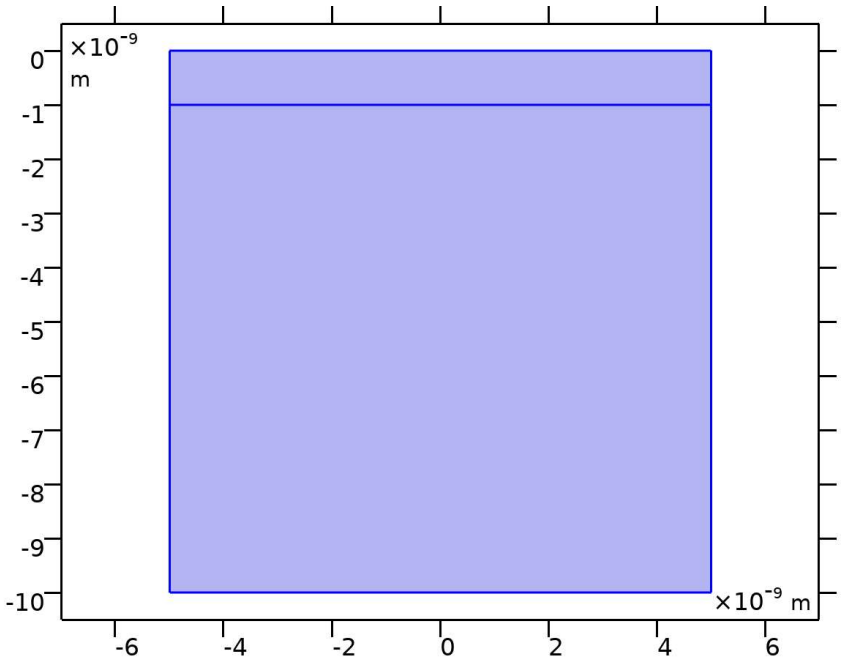

Figure 7.1: The morphology being optimized in FEM simulations

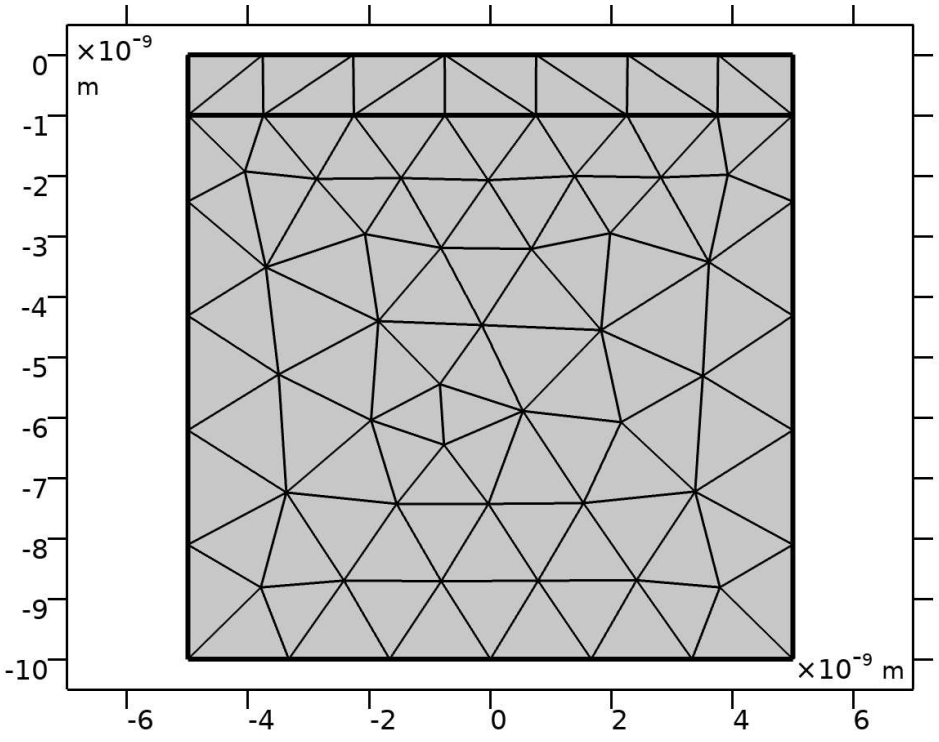

Figure 7.2: The Mesh structure (triangular) being optimized in FEM simulations

The equations' and boundary values being used for FEM simulations.

$$k_1 = \nabla\varphi_1 \quad (7.1)$$

$$\mathrm{E_{T,1}} = \mathrm{E_{T,2}} \quad (7.2)$$

$$\mathrm{n}\times\mathrm{E}=0 \quad (7.3)$$

$$\lambda = -i\beta-\delta_z \quad (7.4)$$

$$\mathrm{H_{T,1}} = \mathrm{H_{T,2}} \quad (7.5)$$

$$\mathrm{n}\times \nabla \times \mathrm{E} - \mathrm{j}\beta\mathrm{n} \times \mathrm{n} = 0 \quad (7.6)$$

$$\mathrm{n}\times (\nabla \times \mathrm{E}) - (\mathrm{jk})\mathrm{n} \times (\mathrm{E} \times \mathrm{n}) = -\mathrm{n} \times \left(\mathrm{E_0} \times \left((\mathrm{ik})\mathrm{n} - \mathrm{jk_1}\right)\right) \mathrm{e}^{-\mathrm{jk1.r}} \quad (7.7)$$

$$(\nabla - j\nabla\emptyset_1) \times \mu_r^{-1}((\nabla - j\nabla\emptyset_1) \times E1) - k_0^2\,(\epsilon_r - \frac{j\sigma}{\omega\epsilon_0})\mathrm{E1}=0 \quad (7.8)$$

$$(\nabla - jk_1) \times \left((\nabla - jk_1) \times E1\right) - k_0^2\epsilon_r\, E1 = 0 \quad (7.9)$$

Further, $CsPbBr_3$ and $CsSnBr_3$ thin films and devices have been prepared by pulsed laser deposition (PLD) technology. Firstly thin films of $CsPbBr_3$ and $CsSnBr_3$ have been prepared and finally, their devices have been synthesized. The $CsPbBr_3$ and $CsSnBr_3$ targets (as an active layer) were synthesized by the cold sintering method.

Thin films and devices of the synthesized sample were fabricated on FTO (fluorine-doped tin oxide) coated glass substrates of size 1.5 x 1.5 cm^2. Acid solutions containing the HCl: H_2O in a 1:1 volume ratio and zinc powder dust were used to etch the substrate. In addition, the shape of the required area of the devices was patterned using nail paint on top of the FTO substrate. After that, acid solution and zinc dust were used to etch the FTO substrates. In

addition, the nail paint of the substrate was removed by immersing it in acetone and the substrate was placed in an ultrasonic bath for 30 min. Finally, these substrates were cleaned in ethanol, deionized water, and acetone using an ultrasonic bath for 30 min for each solution. Organic residues were removed from the cleaned substrates using hot air with a dryer.

To prepare the $CsPbBr_3$ and $CsSnBr_3$ devices, a KrF 248 nm excimer laser was used to bombard the target. TiO_2, active materials ($CsPbBr_3$ and $CsSnBr_3$), CuO thicknesses 200 nm, 200 nm, 250 nm, respectively, were deposited on FTO substrates. The laser pulse numbers for TiO_2, active material, and CuO were 500, 500, and 600, respectively, and with the substrate temperature 150°C.

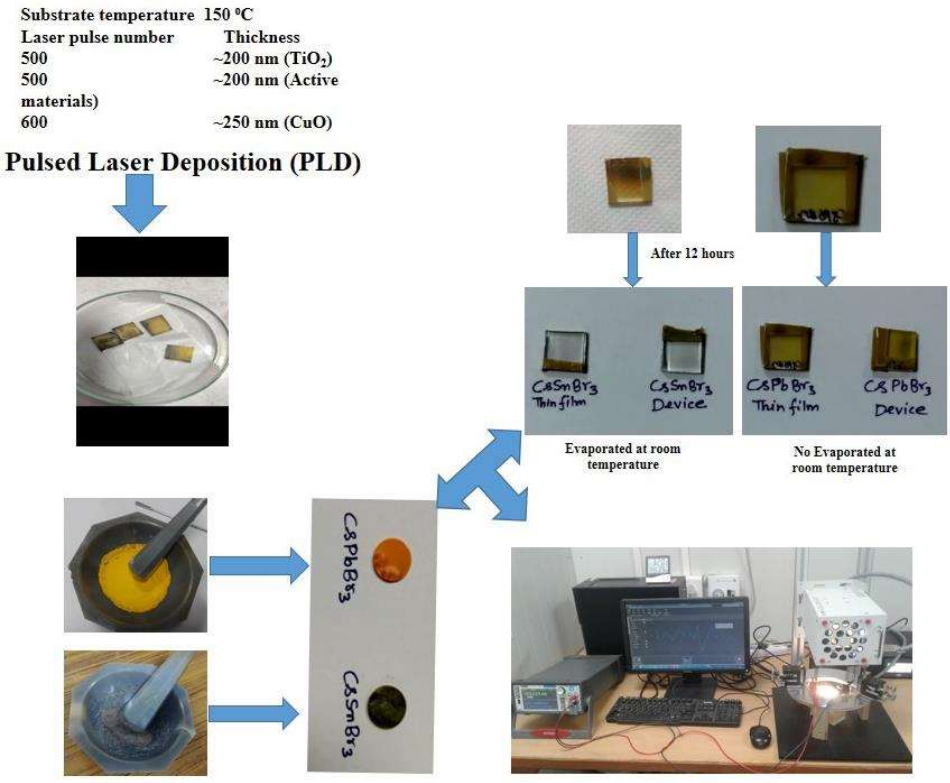

Figure 7.3: $CsPbBr_3$ and $CsSnBr_3$ thin films and devices by PLD techniques at room temperature with the I-V measurements.

7.3 Results and Discussion

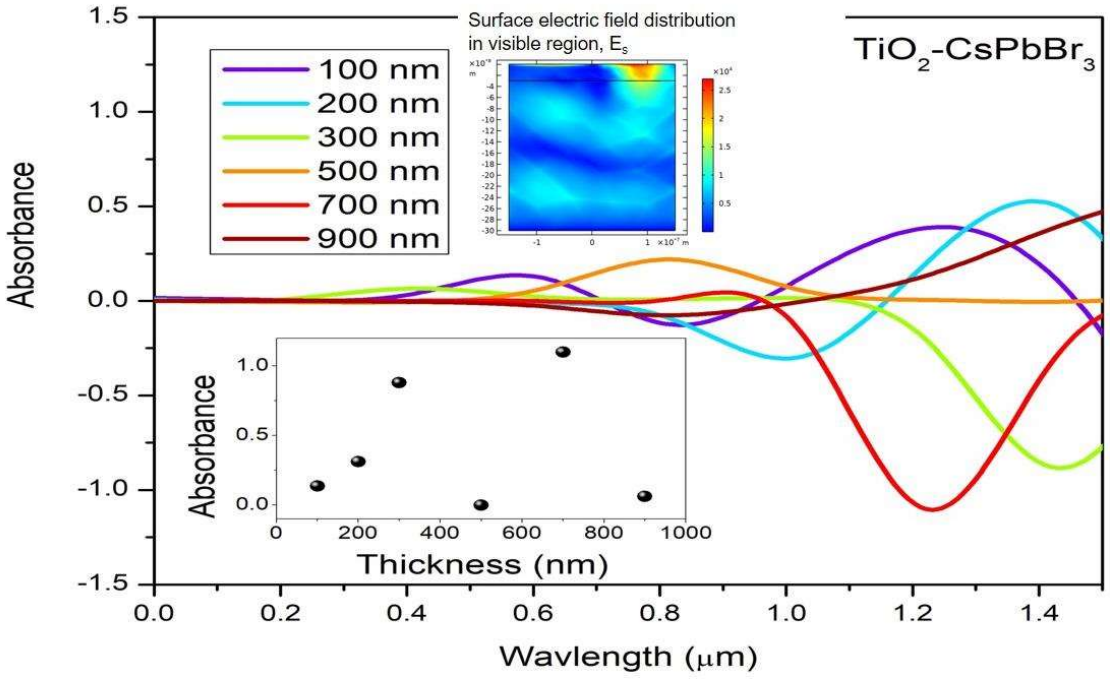

Figure 7.4: Variation of absorbance for $TiO_2/CsPbBr_3$ heterostructure in the wavelength range (0.01- 1.4 μm) inset (i) nearly 100% absorption is obtained for 700 nm thickness for $CsPbBr_3$ and 70 nm thickness of TiO_2 (ii) Surface electric field distribution in the visible region for 300nm thickness of $CsPbBr_3$.

Figure 7.4 demonstrates the variation of absorbance for $TiO_2/CsPbBr_3$ heterostructure in the wavelength range (0.01- 1.4 μm) inset (i) nearly 100% absorption is obtained for 700 nm thickness for $CsPbBr_3$ and 70 nm thickness of TiO_2 (ii) Surface electric field distribution in the visible region for 300 nm thickness of $CsPbBr_3$. It is observed that there is a variation in absorption peak from UV to visible and NIR region. At 100 nm thickness, a broad intense peak is observed in the NIR region instead of a small peak in the visible region. At 200 nm, a peak is observed in the NIR region. At 700 nm thickness, absorption is maximum in the NIR region and for 900 nm thickness, no absorption peak is there. In addition to it, a feeble hump is there for 500 nm thickness.

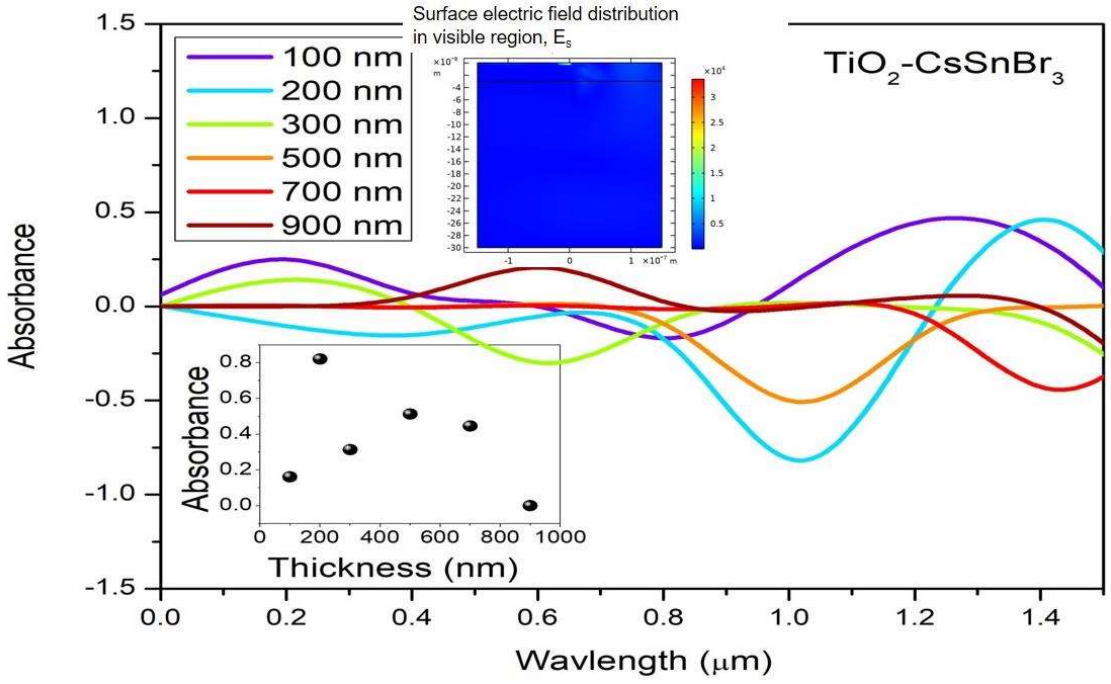

Figure 7.5: Variation of absorbance for $TiO_2/CsSnBr_3$ heterostructure in the wavelength range (0.01- 1.4 μm) inset (i) nearly 80% absorption is obtained for 200 nm thickness for $CsSnBr_3$ and 20 nm thickness of TiO_2 (ii) Surface electric field distribution in the visible region for 300 nm thickness of $CsSnBr_3$.

Figure 7.5 demonstrates the variation of absorbance for $TiO_2/CsSnBr_3$ heterostructure in the wavelength range (0.01- 1.4 μm) inset (i) nearly 80% absorption is obtained for 200 nm thickness for $CsSnBr_3$ and 20 nm thickness of TiO_2 (ii) Surface electric field distribution in the visible region for 300 nm thickness of $CsSnBr_3$. It is observed that there is a variation in absorption peak from UV to visible and NIR region. At 100 nm thickness, 20% absorption is observed in the visible region. At 200 nm, 80% absorption is observed in the NIR region. At 700 nm thickness, absorption is observed in the NIR region and for 900 nm thickness, no absorption peak is there. In addition to it, 50% absorption is observed for 500 nm thickness.

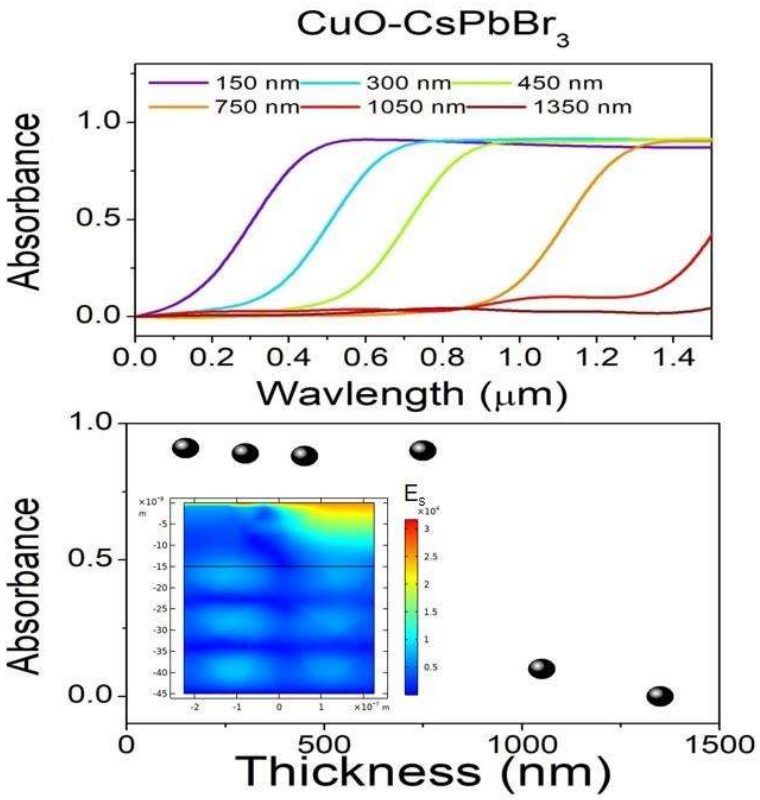

Figure 7.6: (a) Variation of absorbance for CuO/$CsPbBr_3$ heterostructure with thickness in the wavelength range (0.01- 1.4 μm) (b) 98% absorption is obtained for 150 nm – 750 nm thickness for $CsPbBr_3$ and 50 nm – 250 nm thickness of CuO (b inset) Surface electric field distribution in the visible region for 300 nm thickness of $CsPbBr_3$.

Figure 7.6 (a) demonstrates the variation of absorbance for CuO/$CsPbBr_3$ heterostructure with thickness in the wavelength range (0.01- 1.4 μm) (b) 98% absorption is obtained for 150 nm – 750 nm thickness for $CsPbBr_3$ and 50 nm – 250 nm thickness of CuO (b inset) Surface electric field distribution in the visible region for 300 nm thickness of $CsPbBr_3$. It is observed that there is a variation in absorption peak from UV to visible and NIR region with the variation in thickness. At 150 nm thickness of $CsPbBr_3$ and 50 nm thickness of CuO, 98% absorption is observed in the UV region. At 300 nm - 450 nm thickness of $CsPbBr_3$ and 100 nm – 150 nm thickness of CuO, 98% absorption is observed in the visible region. At 750 nm thickness of $CsPbBr_3$ and 250 nm thickness of CuO, 98 % absorption is observed in the NIR region. Further,

for 1050 nm thickness of $CsPbBr_3$ and 350 nm thickness of CuO, no absorption peak is there in the solar spectrum range. Even for 1350 nm thickness of $CsPbBr_3$ and 450 nm thickness of CuO, no absorption peak is there in the solar spectrum range.

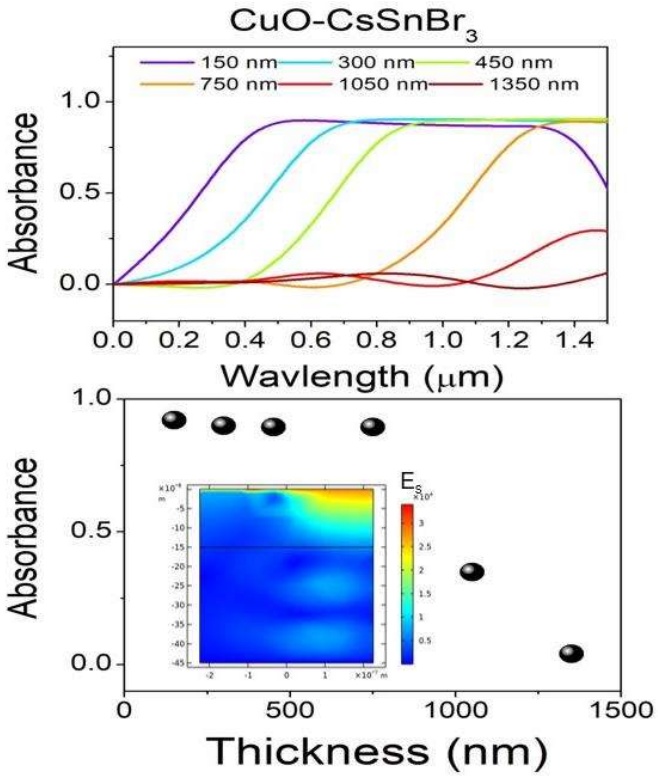

Figure 7.7: (a) Variation of absorbance for CuO/ $CsSnBr_3$ heterostructure with thickness in the wavelength range (0.01- 1.4 μm) (b) 98% absorption is obtained for 150 nm – 750 nm thickness for $CsSnBr_3$ and 50 nm – 250 nm thickness of CuO (b inset) Surface electric field distribution in the visible region for 300 nm thickness of $CsSnBr_3$.

Figure 7.7 (a) demonstrates the variation of absorbance for CuO/$CsSnBr_3$ heterostructure with thickness in the wavelength range (0.01- 1.4 μm) (b) 98% absorption is obtained for 150 nm – 750 nm thickness for $CsPbBr_3$ and 50 nm – 250 nm thickness of CuO (b inset) Surface electric field distribution in the visible region for 300 nm thickness of $CsSnBr_3$. It is observed that there is a variation in absorption peak from UV to visible and NIR region with the variation in thickness. At 150 nm thickness of $CsSnBr_3$ and 50 nm thickness of CuO, 98% absorption is

observed in the UV region. At 300 nm - 450 nm thickness of $CsSnBr_3$ and 100 nm – 150 nm thickness of CuO, 98% absorption is observed in the visible region. At 750 nm thickness of $CsSnBr_3$ and 250 nm thickness of CuO, 98 % absorption is observed in the NIR region. Further, for the 1050 nm thickness of $CsSnBr_3$ and 350 nm thickness of CuO, an absorption peak is observed beyond NIR in the solar spectrum range. Even for 1350 nm thickness of $CsSnBr_3$ and 450 nm thickness of CuO, no absorption peak is there in the solar spectrum range.

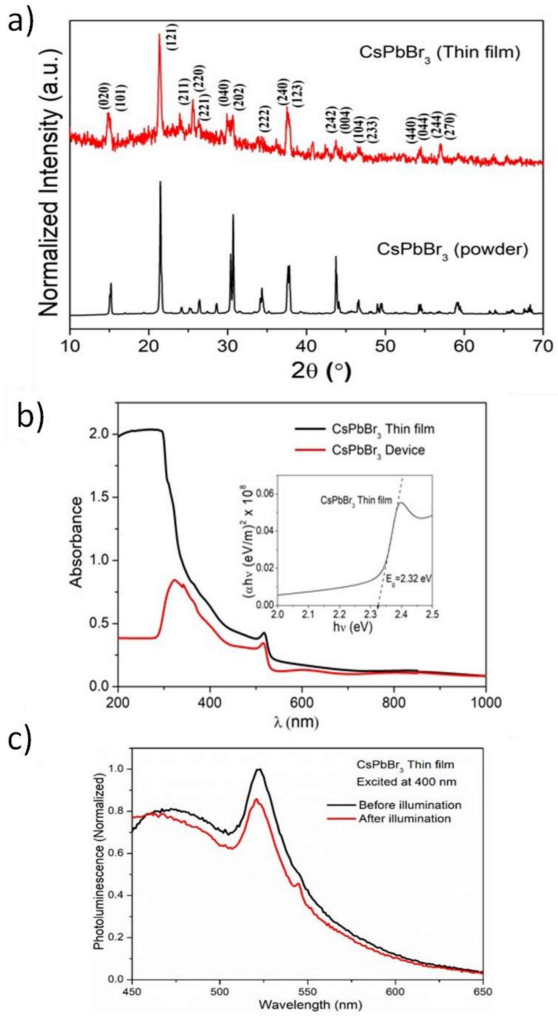

Figure 7.8: (a) XRD patterns of CsPbBr3 powder and their thin film. (b) Absorbance spectra of CsPbBr3 thin films and device. Bandgap plot in insets. (c) Photoluminescence spectrum.

It is observed that the thin films and devices of $CsPbBr_3$ are more stable than that of $CsSnBr_3$ at room temperature (as shown in Fig. 7.3). It is found that the $CsSnBr_3$ thin films and devices rapidly evaporated at room temperature. Therefore, we could not analyze $CsSnBr_3$ thin films and devices with good results. However, the XRD pattern and absorption spectrum of the $CsPbBr_3$ thin-film matches that bulk $CsPbBr_3$. Furthermore, the photoluminescence spectra of the $CsPbBr_3$ thin film were recorded with an excitation wavelength of 400 nm before and after exposure to AM 1.5 G sunlight. It is observed that after light fall, the intensity has reduced showing the reduction of surface state density and unpinned Fermi levels on light exposure.

Table 7.1: ITO/PEDOT:PSS/polyTPD/$CH_3NH_3PbI_3$/PCBM60/Au at different perovskite thicknesses

Thickness [nm]	**Absorbance**	**J_{SC} [mA/cm^2]**	**V_{OC} [V]**	**FF [%]**	**PCE [%]**	**Reference**
$CH_3NH_3PbI_3$						**[196]**
210	0.75	14.7	1.04	0.56	8.6	
250	-	16.7	1.04	0.61	10.6	
285	-	18.8	1.07	0.63	12.7	
370	0.9	18.5	0.97	0.52	9.3	
390	0.92	18.2	1.03	0.46	8.6	
680	-	19.5	0.94	0.44	8.1	
900	1.0	19.5	0.94	0.65	12	
$CsSnBr_3$						
150	0.92					
300	0.9					
450	0.895					

750 1050 1350	0.895 0.348 0.04					
$CsPbBr_3$ 150 300 450 750 1050 1350	 0.91 0.89 0.88 0.9 0.1 0					

Table 7.1 has been reported with the experimental data, and showed the current-voltage data at different perovskite thickness. For a device with a perovskite layer thickness of 900 nm, a PCE of 12% was obtained only slightly below that of the best device with a perovskite layer thickness of 300 nm (experimental reported data). In the present work, through FEM simulations, we have observed that almost 100% absorption is achieved with 700 nm thickness for $CsPbBr_3$ and 70 nm thickness of TiO_2. About 80% absorption is obtained for 200 nm thickness for $CsSnBr_3$ and 20 nm thickness of TiO_2. Therefore, this simulation study will be useful for experimental data.

7.4 Conclusion

The $CsPbBr_3$ thin film is more stable than $CsSnBr_3$ at room temperature. Higher current is observed in $CsPbBr_3$ thin-film whereas, in $CsSnBr_3$ thin film, the sample degrades. Through FEM simulation, $TiO_2/CsSnBr_3$ showed absorbance ~80% for 200 nm thickness. While $TiO_2/CsPbBr_3$ with 700 nm thickness has shown ~100% absorbance (This might be the reason

for higher current). At CuO/$CsPbBr_3$ and CuO/$CsSnBr_3$ interface, both have the same absorbance but electric field distribution is different. ETL/perovskite plays a role in the I_{sc} rather than HTL/perovskite interface. This theoretical study will help to understand the interfaces such as ETL/perovskite and HTL/perovskite problems.

Chapter 8

Conclusions and Future Scopes

CHAPTER 8: Conclusions and Future Scopes

8.1 Conclusion of the Present Investigation

In the present thesis work, low-cost material and the easiest method were used to synthesize perovskite and Ruddlesden-Popper (RP) halides for perovskite solar cells (PSC) applications under ambient conditions such as air and room temperature. As discussed in Chapter 1, it is well known that there are two major problems, the first being stability issues and the second being current-voltage hysteresis issues. The main objective of the thesis work was to resolve the stability issues and to investigate the current-voltage hysteresis to understand the two major problems. Therefore, it was planned to synthesize cesium lead halide $CsPbBr_xI_{3-x}$ (x= 0.0 - 3.0 at the step of 0.5), cesium lead-free halides ($CsSnBr_3$), Ruddelsden-Popper (RP) (Cs_2PbBr_4 and Cs_2SnBr_4) and discussed the stability and degradation mechanisms. In addition, a comparative study of the perovskite and RP material was performed to investigate the I–V hysteresis. Based on the work done, the results obtained and the conclusion presented in the previous chapters after discussion, the overall conclusion of the thesis work can be summarized as follows:

1. The inorganic cesium lead halide $CsPbX_3$ (where X= I, Br, Cl) are reported to possess good stability than that of organic-inorganic hybrid halides. $CsPbI_3$ is reported to have four phases: perovskite black phase (cubic (α), tetragonal (β), orthorhombic(γ)) and non-perovskite yellow orthorhombic (δ). With a band gap of ~ 1.73eV, $CsPbI_3$-α is the most suitable phase among all-inorganic lead halide Perovskites. However, in the ambient atmosphere (almost instantly) the perovskite black phase converts into a non

perovskite yellow orthorhombic phase. At the same time, $CsPbBr_3$ remains in the orthorhombic phase at room temperature. Thus, in the present investigation, the $CsPbBr_xI_{3-x}$ (x= 0.0, 0.5, 1.0) compounds prepared by the cold sintering are observed to be a double phase with P*nma*+ $R\bar{3}m$ symmetry in yellow non-perovskite phase. The XRD patterns showed the orthorhombic phase for $CsPbBr_3$. Further, $CsPbBr_xI_{3-x}$ ($x \leq 1.0$) have shown double phase corresponding to Pnma+ $R\bar{3}m$ symmetry. However, the compound with $1.5 \leq x < 3.0$ showed the presence of various phases with and without oxygen including the $CsPbBr_3$ (orthorhombic, Pnma) phase which has also been confirmed through UV-visible spectroscopy, impedance, and Schottky anomaly. With the incorporation of Br, I sites are occupied by Br^- ions leading to the creation of positive $V_I^{\bullet}$, I incorporation at A – site (Cs) leaving space for the formation of PbI_2 and PbO as confirmed from Raman analysis. From XPS analysis for oxygen, the area corresponding to the metal-OH peak is steadily increasing with x but for $1 \leq x \leq 2$, the area corresponding to the metal-O peak is nearly constant i.e. transforming from Pb-I-influenced region to Pb-O influenced region. This interaction is depending on the I/Br ratio which is also leading to some other by-products and leading this reaction to a typical irreversible reaction.

2. Synthesis and stability are major concerns for these materials. The major work on these materials has been done in inert atmosphere, which is just against the primary criterion of cost effective solar cell materials. The synthesis of halide perovskite thin film is still difficult despite the availability of many synthesis techniques. But, contrary to it, in our very first attempt it is found that sample can be synthesized in the ambient environment through SSR technique and hence low cost synthesis as compared to the other reported

synthesis methods in inert atmosphere has been achieved. Further, the synthesized material can withstand with duration over the changing environment. Hence, it's not intrinsic instability which governs the formation. The samples synthesized through cold sintering method are favored thermodynamically as there entropy is constant. The band gap energy observed for these two samples synthesized with other significant methods indicates that the value is smallest for the samples prepared by cold sintering. Moreover, $CsPbBr_3$ is more stable than $CsPbI_3$ on exposure to AM 1.5G sunlight.

3. Cesium lead iodide material was synthesized by cold sintering method via solid-state reaction (SSR) route. The relaxation time, τ, observed is in the range of 10^{-4} to 10^{-5} sec suggesting the migration of I^- ions at the interstitial sites or its antisites. In the Pb- poor conditions, firstly, V_{Pb} vacancies are created (0.801eV) at low temperature and then V_I vacancies are created (0.534 eV) at high temperature. It is concluded that the activation energy for grain is lower than the grain boundary which indicates to increase in the scattering of charge carriers that are present at the grain boundary. Further, in the low-temperature regime, the activation energy observed from conductivity measurement is different from the relaxation mechanism. Thus, the formation of point defects leads to different conduction and relaxation mechanisms.
4. For the perovskite halides, current-voltage hysteresis is the biggest puzzle to be solved before industrialization in spite of promising features for future photo-voltaic applications. All the possible causes, from the classical (viz., morphology, defects, slow transient capacitance, etc.) to quantum (viz., spin-orbit interaction) ones, are investigated. However, its origin is still under debate, as possibilities showed some ambiguity on the science known until now. In the present work, the time-dependent

photo-conduction behavior of $CsPbBr_3$ in continuous illumination of AM 1.5 G Sunlight for 3 h. It was observed that a negative differential resistance for a forward scanned current-voltage curve in AM 1.5 G Sun light. The defect centers, for example, interstitial Pb^{+2}, act as a mobile generating center, which under the combined action of photo- and space charge limited injection can capture electrons from excitons and provide a free hole for conduction. This Pb^{+2} and holes moving in the same direction with the momentum increase in the forward scan, where the possibility of carrier enhancement at the energy level of traps is possible. It results in the negative differential resistance in the forward scan. However, in the reverse scan, the momentum gets decreased, ion migration is not able to maintain its momentum, and hence, the possibility of carrier enhancement reduces. It appears that reported mechanisms of the hysteresis, i.e., trapping–detrapping, ion migration, polarization, and slow capacitive current, are interrelated. The photo-current voltage hysteresis is primarily affected by the thermionic-field emission (caused by the infrared light part of Sunlight with $h\nu < E_g$), which slows down the drift velocity of hot charge carriers with field applications (forward scan) and could not affect significantly in the reverse scan. Furthermore, it would be interesting to investigate whether this drift velocity slowdown is related to domain conduction (Gunn effect) or momentum-dependent splitting of spin bands (Rashba effect).

5. All compounds ($CsPbBr_3$, $CsSnBr_3$, Cs_2PbBr_4, and Cs_2SnBr_4) were prepared by Cold sintering (CS)–Solid-state reaction (SSR) route. It is observed that the polarization is higher in RS than FS in ‘Sn’ samples irrespective of the structure. But polarization is higher in FS than in ‘Pb’ samples irrespective of the structure. It can be concluded that the 'Pb' based sample has an order of 1000 difference in polarization as compared to

the Sn-based samples. It is also observed that the polarization of cesium lead bromide ($CsPbBr_3$) material is in the range of 10^0, due to which it has minimum I-V hysteresis.

6. The $CsPbBr_3$ thin film is more stable than $CsSnBr_3$ at room temperature. Higher current is observed in $CsPbBr_3$ thin-film whereas, in $CsSnBr_3$ thin film, the sample degrades. Through FEM simulation, $TiO_2/CsSnBr_3$ showed absorbance ~80% for 200 nm thickness. While $TiO_2/CsPbBr_3$ with 700 nm thickness has shown ~100% absorbance (This might be the reason for higher current). At $CuO/CsPbBr_3$ and $CuO/CsSnBr_3$ interface, both have the same absorbance but electric field distribution is different. ETL/perovskite plays a role in the I_{sc} rather than HTL/perovskite interface. This theoretical study will help to understand the interfaces such as ETL/perovskite and HTL/perovskite problems.

Overall, it can be concluded $CsPbBr_3$ was found to be the most stable compound among all the synthesized materials with the minimum hysteresis.

8.2 Future Scope

Some of the following points may be noted for future prospects in this field.

- Develop the material for faster optoelectronic switching devices, photodetectors along with solar cells.
- Improving the performance and stability of devices with parameters such as J_{sc}, V_{oc}, *FF,* and *PCE* may be optimized.
- The time scale required for the redistribution of the mobile ions, the interaction between ion migration and electrode polarization, how the interfacial photo-electrons/ holes with

trapped charges and mobile ions create an impact on the capacitive current, and band bending, that are required to be investigated.

- Time-dependent electrical studies for perovskite and Rudlesden–Popper (RP) materials and fabrication of thin films in the form of devices are needed.

- The localization length and mean free path of the carrier are needed for the $CsPbBr_3$ compound.